

Supplementary Information

Observation of Kondo hybridization with an orbital-selective Mott phase in $4d$ $\text{Ca}_{2-x}\text{Sr}_x\text{RuO}_4$

Supplementary 1: Intensity normalization for the ARPES data

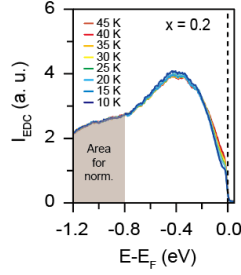


Fig. S1. T -dependent integrated EDCs for $x = 0.2$ and the EDC area for normalization. Temperature-dependent integrated energy distribution curve (EDC) from region #1 ($0.6 < k_x (\text{\AA}^{-1}) < 0.8$) in Fig. 2a. The brown-shaded area indicates the area for intensity normalization.

To compare the doping- and T -dependent results, the intensity of the angle-resolved photoemission spectroscopy (ARPES) data must be normalized in a systematic way. For accurate comparison, a normalization area is selected in which bands do not cross. To obtain the normalization factor, we plotted momentum-integrated EDCs near the S point ($0.6 < k_x (\text{\AA}^{-1}) < 0.8$, region #1 in Fig. 2) as shown in Fig. S1. In addition, the binding energy (BE) region between 0.8 and 1.2 eV is selected for normalization since this region has negligible doping- or T -dependences. In brief, all the ARPES data (doping- and T -dependent) are intensity normalized with the region ($0.6 < k_x (\text{\AA}^{-1}) < 0.8$, $-1.2 < E-E_F$ (eV) < -0.8).

Supplementary 2: Doping-dependent evolution of orbital-selective Mott phase

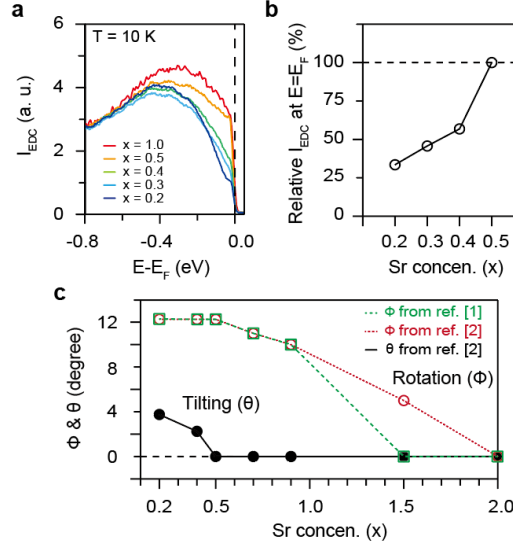


Fig. S2. Doping (x)-dependent evolution of orbital-selective spectral weight suppression. (a) Plot for momentum-integrated EDCs (region #1, $x = 1.0, 0.5, 0.4, 0.3$ and 0.2) and (b) x -dependent spectral weight intensity ratio (compared to $x = 0.5$) at the Fermi energy (E_F) extracted from (a). (c) Plot of x -dependent RuO_2 octahedral rotation (Φ , open square¹ and circle²) and tilting (θ , solid circle²) angles obtained from references [1, 2].

The x -dependent evolution of the orbital-selective Mott phase (OSMP) in the γ -band is shown in Fig. S2. In Fig. S2(a), the OSMP driven soft gap opens and the spectral weight around E_F is gradually suppressed from $x = 0.5$ to 0.2 . The OSMP gap size seems to be around 0.4 eV where the EDC peak increases with spectral weight transfer. To demonstrate the gradual evolution of OSMP, x -dependent spectral weight ratios (compared to $x = 0.5$, critical point of OSMP) at E_F are plotted in Fig. S2(b). Stronger suppression of the spectral weight indicates strengthened OSMP. As shown in Fig. S2(c) (x -dependent octahedral rotation / tilting angles^{1,2}), the strength of the OSMP (spectral weight suppression of the γ -band) seems to be proportional to the tilting angle.

On the other hand, the EDC at $x = 1.0$ does not show Mott-like (lower to higher BE) spectral weight transfer as well as spectral weight suppression around the E_F (Fig. S2(a)). Since the octahedral tilting angle is zero and the rotation angle varies in the region between $x = 0.5$ and 1.0 (Fig. S2(c)), we conclude that the OSMP does not occur only with octahedral rotation, hence octahedral tilting is the key to

triggering the OSMP.

Supplementary 3: Temperature-dependent evolution of orbital-selective Mott phase

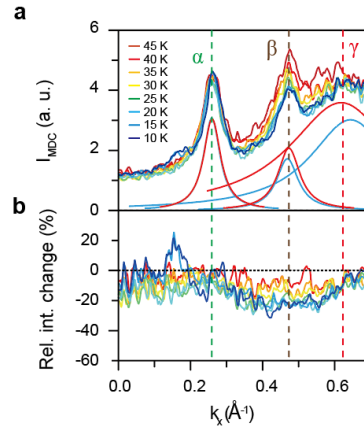


FIG. S3. Temperature (T)-dependent evolution of orbital-selective spectral weight suppression. (a)

T -dependent normalized momentum distribution curves (MDCs) of $x = 0.2$ at E_F (± 10 meV) along Γ -S.

The coloured solid lines are fitted Lorentzian functions of the α -, β - and γ -bands from MDCs measured at 15 K (blue) and 45 K (red). The coloured dashed lines indicate the k_F position of each band. **(b)** T -

dependent relative intensity changes in MDCs compared to 45 K.

The T -dependent MDCs exhibit orbital-selective spectral weight suppression at E_F . As can be seen in Fig. S3(a), the β - and γ -bands show spectral weight suppression, but the α -band remains almost unchanged.

The T -dependent orbital selectiveness is more clearly seen in Fig. S3(b), which shows the MDCs subtracted from that of 45 K.

Supplementary 4: Electric and magnetic properties of $\text{Ca}_{2-x}\text{Sr}_x\text{RuO}_4$ ($0.2 \leq x \leq 0.5$)

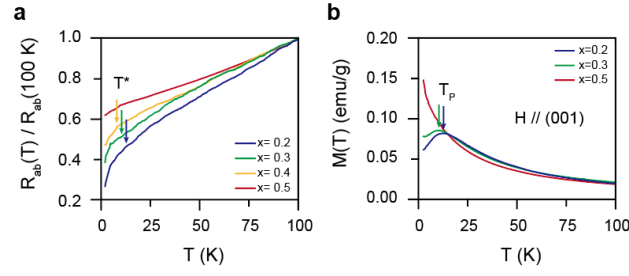


Fig. S4. In-plane resistivity and magnetic property data of $\text{Ca}_{2-x}\text{Sr}_x\text{RuO}_4$ (CSRO) ($0.2 \leq x \leq 0.5$). Measured T -dependent plots for (a) in-plane resistivity normalized at $T = 100$ K and (b) magnetization measured with an applied magnetic field (0.1 Tesla) along the c -axis (001). The coloured arrows indicate the reported values of T^* (incoherent to coherent crossover temperature) and T_P (peak temperature in magnetic susceptibility), respectively, obtained from references [3-7].

To characterize the physical properties of our bulk CSRO crystals, the T -dependent in-plane resistivity with the 4-probe method and magnetization with an applied magnetic field along the c -axis were measured using a physical property measurement system (PPMS) and a magnetic property measurement system (MPMS), respectively (Fig. S4). Our results (consistent with previous studies³⁻⁷) show characteristic temperatures, the incoherent to coherent crossover temperature (T^* , in resistivity) and the antiferromagnetically driven peak temperature (T_P , in magnetic susceptibility). These T -dependent slope changes (below/above T^* and T_P) in resistivity and magnetic susceptibility are observed in various HF d -electron⁸⁻¹⁰ as well as f -electron¹¹⁻¹⁵ systems, related to the hybridization between localized and conduction electrons⁸⁻¹⁵. This strongly suggests a possible Kondo-hybridization (KH) scenario in CSRO.

Supplementary 5: The effect of octahedral distortions on the electronic structure of CSRO

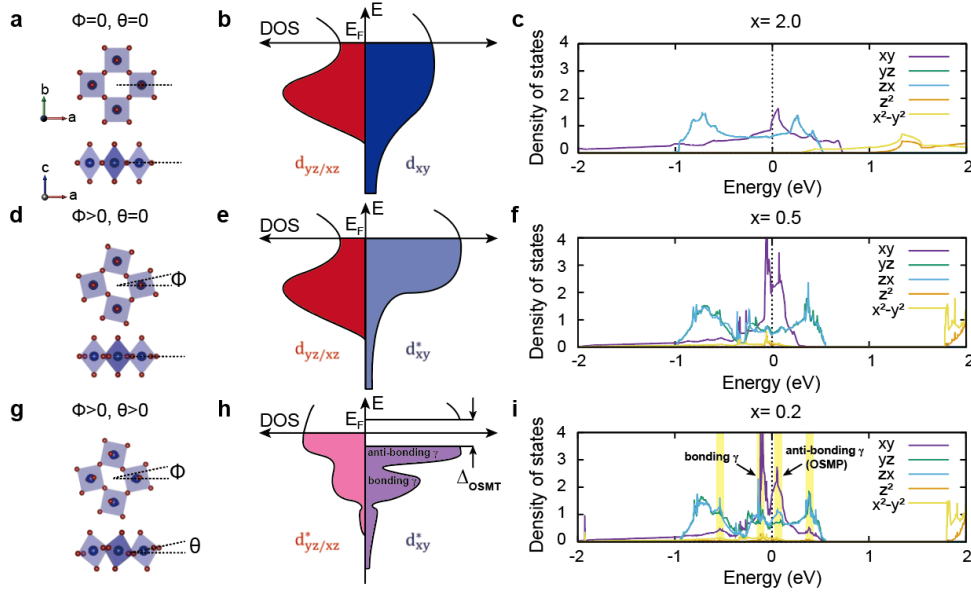


Fig. S5. Effect of octahedral distortions on the electronic structure of CSRO. **(a,d,g)** Top and side view of crystal structures in CSRO **(a)** without distortion ($1.5 \leq x \leq 2.0$), **(d)** with rotation along the c -axis ($0.5 \leq x < 1.5$) and **(g)** with both rotation and tilting ($0.0 \leq x < 0.5$). **(b,e,h)** Schematic electronic structural changes corresponding to each distortion types: **(b)**, **(e)**, and **(h)** corresponds to **(a)**, **(d)**, and **(g)**, respectively. **(c,f,i)** Orbital-dependent ($4d$) density of states (DOS) at **(c)** $x = 2.0$, **(f)** $x = 0.5$, and **(i)** $x = 0.2$ from first-principles density functional theory (DFT) calculations. Yellow shaded regions indicate the binding energy region in which d_{xy} and $d_{yz/xz}$ have a coincident DOS peak.

Octahedral distortions (rotation/tilting) create a narrower bandwidth in d -orbitals; the detailed explanation of the mechanism is as follows. Without octahedral rotation/tilting, $4d$ orbitals (three t_{2g} and two e_g) of Sr_2RuO_4 possess a wide bandwidth (Fig. S5(a-c)). Once octahedral (in-plane) rotation occurs, the d_{xy} and $d_{x^2-y^2}$ orbitals become hybridized, which leads to a bandwidth reduction in the γ (d_{xy}^*) band¹⁶ while the $d_{yz/xz}$ orbitals remain almost intact (Fig. S5(d-f)). The role of octahedral rotation in band structure is well-known, but the role of octahedral tilting is not yet clearly understood.

As shown in Fig. S2, there are coincident and proportional behaviours between octahedral tilting and the OSMP. To investigate the role of octahedral tilting in band structure, we performed DFT calculations for $x = 0.2$ (with octahedral rotation/tilting; Fig. S5(i)). There are several energy regions (yellow shaded area

in Fig. S5(i)) in which d_{xy} and $d_{yz/zx}$ have a coincident DOS peak, in contrast to the case without octahedral tilting (Fig. S5(c,f)). These coincidences suggest that d_{xy} and $d_{yz/zx}$ are mixed and hybridized. The hybridization between d_{xy} and $d_{yz/zx}$ will create divisions in bands with narrow bandwidths, similar to how octahedral rotation narrows the bandwidth of d_{xy} ¹⁶.

Supplementary 6: Breakdown of the OSMP induced by electron doping from alkali metal (K) evaporation

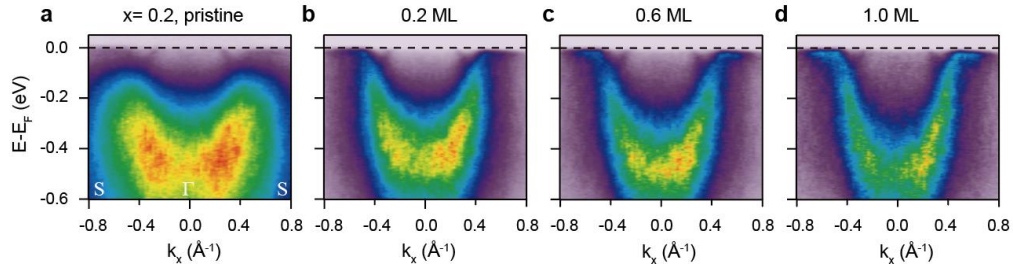


Fig. S6. Breakdown of the OSMP with K evaporation. (a-d) ARPES images along S- Γ -S of $x = 0.2$ measured with σ -polarized light with K **(a)** 0, **(b)** 0.2, **(c)** 0.6 and **(d)** 1.0 monolayer (ML) coverage.

Alkali metal evaporation is widely used to impart an electron-doping effect on a crystal²⁰. A previous ARPES study on Sr_2IrO_4 ²¹ showed that additional electrons from potassium (K) lead to the sudden breakdown of the Mott-localized state. Motivated by this work²¹, we performed electronic structure measurements with K evaporation to determine whether the OSMP in CSRO ($x = 0.2$) breaks down in the same way as the Mott state in Sr_2IrO_4 . As shown in Fig. S6, the OSMP soft gap becomes closed with infinitesimal K coverage (< 0.2 ML), and exhibits recovered dispersive bands. This implies that the origin of spectral weight suppression in the γ -band is Mott-localization.

Supplementary 7: Doping-dependent electron occupancies in each band

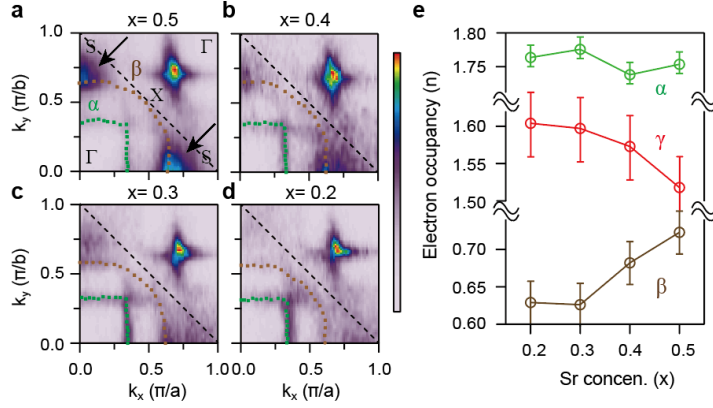


Fig. S7. x -dependent FSs and electron occupancies. (a-d) Fermi surfaces (FSs) of (a) $x = 0.5$, (b) 0.4, (c) 0.3, and (d) 0.2. As x decreases from 0.5 to 0.2, the γ -band intensity (arrow) weakens and eventually disappears (OSMP). Coloured dots indicate FS contours of the α - (green) and β - (brown) bands obtained from a Lorentzian fit of MDCs. Black dashed lines indicate the reduced Brillouin zone (BZ) due to octahedral distortions. (e) The electron occupancies of each band are plotted as a function of Sr concentration extracted from Luttinger's theorem²². Since the γ -band occupancies cannot be directly obtained due to the OSMP, they are calculated by subtracting the α - and β -band occupancies from 4.

Half-filled electron occupancy is essential for Mott localization. In Fig. S7(e), we extracted the electron occupancies of each band. The γ -band at $x = 0.5$ has about 1.5 electrons, which satisfies the half-filled condition in the doubled unit cell picture¹⁷, while the other α (1.8) and β (0.7) bands are far from the half-filled condition. The electron occupancy of the β -band decreases from $x = 0.5$ to 0.2. This behaviour is likely due to the KH-induced band renormalization.

Supplementary references

- [1] Friedt, O. et al. Structural and magnetic aspects of the metal-insulator transition in $\text{Ca}_{2-x}\text{Sr}_x\text{RuO}_4$. *Phys. Rev. B* **63.17**, 174432 (2001).
- [2] Noh, H. J. et al. Electronic structure and evolution of the orbital state in metallic $\text{Ca}_{2-x}\text{Sr}_x\text{RuO}_4$. *Phys. Rev. B* **72.5**, 052411 (2005).
- [3] Nakatsuji, S. & Maeno, Y. Switching of magnetic coupling by a structural symmetry change near the Mott transition in $\text{Ca}_{2-x}\text{Sr}_x\text{RuO}_4$. *Phys. Rev. B* **62**, 6458-6466 (2000).
- [4] Nakatsuji, S., & Maeno, Y. Quasi-two-dimensional Mott transition system $\text{Ca}_{2-x}\text{Sr}_x\text{RuO}_4$. *Phys. Rev. Lett.* **84.12**, 2666-2669 (2000).
- [5] Nakatsuji, S. et al. Heavy-mass Fermi liquid near a ferromagnetic instability in layered ruthenates. *Phys. Rev. Lett.* **90.13**, 137202 (2003).
- [6] Carlo, J. P. et al. New magnetic phase diagram of $(\text{Sr,Ca})_2\text{RuO}_4$. *Nat. Mater.* **11.4** 323-328 (2012).
- [7] Jin, R. et al. Heavy-electron behavior and structural change in $\text{Ca}_{1.7}\text{Sr}_{0.3}\text{RuO}_4$. Preprint at <http://arXiv.org/abs/cond-mat/0112405> (2001).
- [8] Wu, Y. P. et al. Emergent Kondo lattice behavior in iron-based superconductors AFe_2As_2 (A= K, Rb, Cs). *Phys. Rev. Lett.* **116.14**, 147001 (2016).
- [9] Cheng, J. G. et al. Possible Kondo physics near a metal-insulator crossover in the A-site ordered perovskite $\text{CaCu}_3\text{Ir}_4\text{O}_{12}$. *Phys. Rev. Lett.* **111.17**, 176403 (2013).
- [10] Zhang, Y. et al. Emergence of Kondo lattice behavior in a van der Waals itinerant ferromagnet, Fe_3GeTe_2 . *Sci. Adv.* **4.1**, eaao6791 (2018).
- [11] Hegger, H. et al. Pressure-induced superconductivity in quasi-2D CeRhIn_5 . *Phys. Rev. Lett.* **84.21**, 4986 (2000).
- [12] Zapf, V. S. et al. Coexistence of superconductivity and antiferromagnetism in $\text{CeRh}_{1-x}\text{Co}_x\text{In}_5$. *Phys. Rev. B* **65.1**, 014506 (2001).
- [13] Ōnuki, Y. et al. Dense Kondo Behavior in $\text{Ce}_x\text{La}_{1-x}\text{Al}_2$. *J. Phys. Soc. Jpn.* **53.8**, 2734-2740 (1984).

- [14] Gottwick, U. et al. Seebeck coefficient of heavy fermion compounds. *J. Magn. Magn. Mater.* **63**, 341-343 (1987).
- [15] Bel, R. et al. Giant Nernst effect in CeCoIn₅. *Phys. Rev. Lett.* **92.21**, 217002 (2004).
- [16] Ko, E., Kim, B. J., Kim, C., & Choi, H. J. Strong orbital-dependent *d*-band hybridization and Fermi-surface reconstruction in metallic Ca_{2-x}Sr_xRuO₄. *Phys. Rev. Lett.* **98.22**, 226401 (2007).
- [17] Neupane, M. et al. Observation of a novel orbital selective Mott transition in Ca_{1.8}Sr_{0.2}RuO₄. *Phys. Rev. Lett.* **103.9**, 097001 (2009).
- [18] Kresse, G., & Joubert, D. From ultrasoft pseudopotentials to the projector augmented-wave method. *Phys. Rev. B* **59.3**, 1758-1775 (1999).
- [19] Kresse, G., & Furthmüller, J. Self-interaction correction to density functional approximation for many electron systems. *Phys. Rev. B* **54**, 11169 (1996).
- [20] Kyung, W. S. et al. Enhanced superconductivity in surface-electron-doped iron pnictide Ba(Fe_{1.94}Co_{0.06})₂As₂. *Nat. Mater.* **15.12**, 1233-1236 (2016).
- [21] Kim, Y. K. et al. Fermi arcs in a doped pseudospin-1/2 Heisenberg antiferromagnet. *Science* **345.6193**, 187-190 (2014).
- [22] Luttinger, J. M. Fermi surface and some simple equilibrium properties of a system of interacting fermions. *Phys. Rev.* **119.4**, 1153-1163 (1960).